Made available through Montana State University's ScholarWorks

Mesoscale magnetically-guided nanoparticle gradients generate spatially heterogeneous neuronal protein expression responses

Mackenna K Landis and Anja Kunze

Accessibility Disclaimer:

For a more accessible version of this document, please submit an accessibility request form through the Montana State University Library website.

Mesoscale magnetically-guided nanoparticle gradients generate spatially heterogeneous neuronal protein expression responses

*Mackenna K Landis[a], Anja Kunze[*a, b, c]*

[a]Department of Electrical and Computer Engineering, Montana State University, Bozeman, Montana 59717, USA.

[b]Montana Nanotechnology Facility, Montana State University, Bozeman, Montana 59717, USA.

[c]Optical Technology Center, Montana State University, Bozeman, Montana 59717, USA.

*Corresponding author: Dr. Anja Kunze; Email:anja.kunze@montana.edu

Keywords: *In vitro gradients, magnetic gradients, neuronal engineering, guided magnetofection*

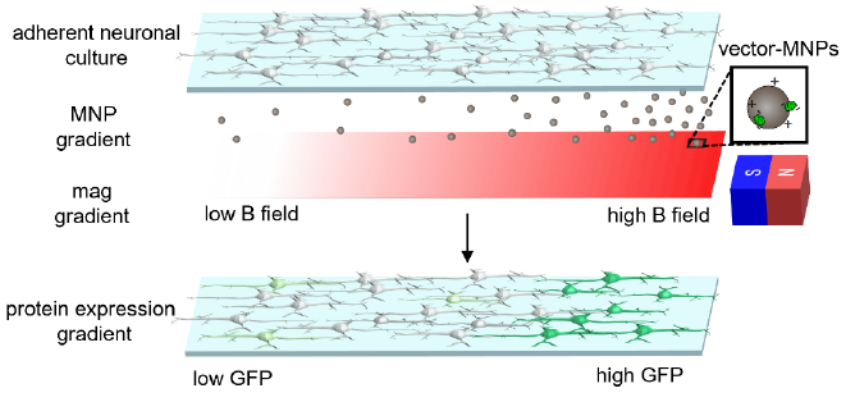
1 Abstract

Spatial signal gradients are ubiquitous throughout *in vivo* tissues, with heterogeneous variables ranging from protein expression to tissue stiffness. Research into the development of biomimetic gradients has led to a wide range of technological advances within this field, with promise to progress tissue engineering for both therapeutic testing as well as tissue regeneration. However, most technologies are limited to the microscale or require complex tools and equipment to generate *in vitro* gradients. Here, we propose a low-cost method for generating *in vitro* meso-scale protein expression gradients using a 3D printed magnetic ring that exerted a spatially heterogeneous magnetic field within a standard 35-mm cell culture dish. We then optimized a method for magnetically guiding viral vectors for localized gene expression enrichment. Finally, we examine the potential for utilizing this platform to generate localized neuronal Ca^{2+} activity alterations.

2 Statement of Significance

Molecular gradients are a critical feature of tissues during development, driving a number of spatially variable biological functions. For example, differentiation of cellular identities is driven by gradients based on spatially variable protein expression across a community of cells. Several technologies have been devised to recapitulate molecular gradients *in vitro*, usually on the microscale. To generate *in vitro* gradients on a larger scale, we introduce a proof-of-concept method using magnetically actuated mechanical force gradients to generate protein expression gradients across a culture of adherent cells. This low-cost mesoscale method could be harnessed to create consistently organized, spatially variable cell identities across cultures of millions of cells.

3 Graphical Abstract



3 Introduction

Spatial gradients of biological signals are a ubiquitous characteristic of biological tissues, with a variety of roles for physiological function. Gradients of growth factors can drive cellular migration [1–3], outgrowth of cellular processes [4–6], and even define patterns of cellular differentiation during tissue development [7–9]. Molecular gradients of morphogens, such as

Wnt and Hedgehog, determine the localized identity of cells that make up anterior/posterior regions during embryonic development [9–11]. These extracellular biochemical gradients, largely driven by diffusion of secreted proteins, then generate tissue-wide gradients of intracellular protein expression [8]. Cells respond to mechanical gradients as well, with stiffness gradients known to play integral roles in axonal targeting [12] and cellular migration [13,14]. Greater characterization of these gradients can both inform knowledge of tissue development [15]. However, traditional *in vitro* cell culture methods often neglect the inclusion of these gradients, requiring dedicated development of novel technologies to facilitate the ubiquitous adoption of gradient formation *in vitro*.

Diverse technologies have been exploited to introduce biomimetic signal gradients to cellular cultures. Fluidic, and especially microfluidic, platforms have often been used to create chemical concentration gradients for cellular migration and reorientation studies [16–19] testing drug candidates [20], and even examining the transmission of neurotoxins [21, 22]. While these devices are highly efficient on the microscale, they generally lose specificity at larger spatial scales. Bioprinting techniques have allowed researchers to pattern cells directly within hydrogel bioinks [26] or to fabricate mechanical and/or chemical gradients within three-dimensional cell scaffolds [27–29]. However, direct cellular bioprinting can be difficult to achieve with sensitive cell types such as neurons [29,30]. The spatial precision of optical systems can take advantage of genetically engineered cells to uncage proteins in specific locations within a genetically engineered cell culture [11,31]. Especially promising *in vivo* solutions include engineered nerve growth conduits which incorporate multifaceted gradients (i.e. both mechanical and chemical) to accelerate guided regrowth of peripheral axons following injury [23–25]. Many of the technologies listed above are highly effective on spatial scales up to a few millimeters but are

difficult to scale beyond this range or require costly and complex equipment. However, the use of remote forces, such as magnetic forces, within a low-viscosity environment, provides an alternative method of generating a biologically relevant signal gradient that can be tuned to numerous spatial scales and provide high throughput, with low economic and training cost.

Magnetically-actuated mechanical forces (nanomagnetic forces, NMF) are a particularly advantageous technology for engineering biological gradients. Magnetic nanoparticles (MNPs) transduce external magnetic fields into mechanical forces as the two magnetic cores interact [32]. Permanent magnets exert an inherent magnetic field gradient, providing a physical tool that could be exploited for biological gradient generation. Permanent neodymium (NdFeB) magnets are relatively inexpensive and simple to rearrange, providing myriad potential gradients without having to fabricate new devices [33–36].

Many studies have utilized these forces to target MNP-labeled cells into precise patterns or regions within a dish [37–39]. MNPs can be functionalized to carry and localize biomolecules or genetic vectors, which increases cellular uptake by bringing those molecules in contact with cells more . This technique, also known as magnetofection, has been utilized for over two decades to increase viral vector efficacy *in vitro* [40,41]. Further, magnetic gradients have been utilized to facilitate selected positioning of morphogens [42] and cells [43] on a millimeter scale within hydrogels. Magnetic particles have also been used to facilitate both mechanical guidance cues as well as remotely controlled drug release for nerve regrowth [25]. Nerve growth factor-functionalized nanoparticles have been employed to facilitate localized PC12 differentiation on a millimeter scale [44]. Our aim was to explore whether NMF could be exploited on an even greater physical scale to generate biological signal gradients on a centimeters-wide cellular culture.

Here, we present a proof-of-concept study for a method to utilize magnetic gradients on the scale of mesoscale (standard 35-mm Petri dishes) to generate 1.5D protein expression gradients without the use of hydrogels or other scaffolds. We first characterize the spatiotemporal variables that enable the magnetic field platform to generate these gradients, then utilize this platform to generate protein expression gradients using guided magnetofection. Finally, we examine how the guided application of MNPs facilitates local changes in neuronal activity.

4 Materials and Methods

4.1 Magnetic field simulations and nanomagnetic force calculation

The force of a magnetic gradient on a particle is defined by the following equation:

$$\boldsymbol{F_{MNP}} = \frac{\Delta\chi V_{MNP}}{\mu_0}(\boldsymbol{B}\cdot\boldsymbol{\nabla})\boldsymbol{B}$$

where the value $\Delta\chi$ is the magnetic susceptibility of the particle relative to the media, V_{MNP} is the volume of the particle, and μ_0 represents the magnetic permeability of free space. The value $\frac{\Delta\chi V_{MNP}}{\mu_0}$, then, represents a constant value that is particular to the material and size of the particle, theoretically independent from the applied field. The term $(\boldsymbol{B}\cdot\boldsymbol{\nabla})\boldsymbol{B}$ is a measure of the direction and strength of the gradient magnetomechanical field (GMF) to which the particle is exposed, with units of $T^2\,m^{-1}$. Within the study, the GMF was generated by a proprietary arrangement of N52 neodymium (NdFeB) permanent magnets within a 3D printed ABS ring (Nanomagnetic Solutions, USA). Magnetic fields imposed by this magnetic ring were simulated *via* finite element modeling on COMSOL Multiphysics 5.6 software (COMSOL AB, Sweden). The GMF magnitude and direction at each point within the finite element model's mesh could then be exported.

4.2 MNP distribution testing

To perform fluorescent imaging of nanoparticle distribution, within the applied magnetic fields, 10 µL FluoMag (OZ Biosciences) was diluted into 2 mL warmed PBS. A PLL-treated 35 mm Petri dish was then placed in the test arrangement (flush with bottom of ring, flush with top of ring, on loft platform 3 mm above top of ring, see Figure S1). Dishes were kept in the magnetic field for 1, 2, 6 or 24 hours of a 24- hour period. Dishes were then fluorescently imaged (Ex:560/40 nm; Em: 610/40 nm) via tile scan using a Leica DMi8 inverted microscope fitted with a Hamamatsu Orca Flash 4.0 digital camera. The tile scan covered a scan of the center axis along which the GMF increased to assess a pseudo-one-dimensional (1.5-dimensional) gradient. Tile scan individual frames were exported without compression as '.tif' files, that were merged on ImageJ FIJI using the Grid Stitching plugin [45]. An intensity threshold was then applied to identify fluorescent MNPs from the merged image, which was dissected into ten regions of interest (ROI) of equal width. FIJI's particle analyzer was then applied on the binary image to identify particles with an area $\geq 0.425\ \mu m^2$. Particle counts were then normalized to the total surface area of the dish contained within each image (ROI 1 and ROI 10 at dish edges contained 97% dish surface area, owing to the curved edges of the dish).

4.3 Cell culture

Primary embryonic rat neurons were cultured as in Landis and Kunze [36]. Briefly, the cortices and hippocampi were separately dissected from both hemispheres of embryonic day 18 (E18) whole rat brains (TransnetYX, Springfield, IL, USA). Cortices and hippocampi were then digested using Papain (Carica Papaya, Roche, USA) for 15 minutes followed by mechanical trituration via pipette in a transfer medium (90% Neurobasal Plus, Gibco, 10% donor equine serum, Cytiva Hyclone). Following mechanical dissociation, cells were strained through a 40 µm

cell filter (CellTreat) to remove large clusters. Finally, cells were centrifuged at 400 rpm for 12-18 minutes to create a cell pellet. The supernatant was then removed and replaced with complete cell medium (97% Neurobasal Plus, 2% B27 Plus, 1% Glutamax). Neuronal cells were counted using a hemocytometer. Cells were then seeded on 0.0025% poly-L-lysine-treated 35 mm Petri dishes (CellTreat, Fisher Scientific, USA). For viral experiments, cortical cells were seeded at a high density of 2M cells per dish. For Ca^{2+} experiments, hippocampal cells were seeded at 1M cells per dish.

4.4 Virus-MNP mixing and transduction

Serotype I Adeno-associated viruses (AAV) with CMV promoter and GFP gene of interest were purchased from Vector Biolabs. Each aliquot contained 1×10^{13} VG/mL. 13 hours prior to transduction, 1 µL of AAV was added to 500 µL, 0.02 mg/mL 250 nm diameter PEI-enhanced gold-coated MNPs (PEI-MNPs, Nanopartz, USA) in PBS, within a 1-dram glass vial. Viruses and PEI-MNPs were pipetted up and down 3x for initial mixing and then placed on an orbital mixer for 12 hours to, covered in foil, to continue mixing and encourage adhesion between MNPs and viruses. Microcentrifuge tubes were then placed on top of 0.6 T neodymium magnets for 10 minutes. Supernatant was removed to wash unattached viruses from mixture and replaced with 500 µL fresh PBS. Mixtures were magnetically washed once more, but the supernatant was then replaced with 1 mL complete cell medium. Virus-MNP mixtures were then placed in 37°C dry bath until addition to cells.

4.5 AAV-MNP guided transduction and fixation

Virus-MNPs were gently agitated by pipetting to resuspend particles and added dropwise around the 35-mm dishes to create even coverage. The side of the dish that was exposed to the

high magnetic field was designated with a vertical line drawn on the side of the Petri dish base. Dishes that were exposed to GMFs were kept within the field for 6 hours. Virus-MNP mixtures were kept in the dish for 24 hours, then washed 3x with warmed complete cell media. Cells were transduced at 7 DIV. Dishes were maintained in complete cell media for 96 hours following the start of the transduction, with media exchanged every 48 hours. Cells were then washed 3x with warmed DPBS (Thermo Fisher, USA) then fixed with 4% formaldehyde in PBS (Thermo Fisher, USA). Cells were washed 3x following fixation, then permeabilized with TBST (0.1% Triton-X (Millipore Sigma, USA), 3% BSA (Millipore Sigma, USA), 1% PenStrep (Thermo Fisher, USA) in DPBS) for 10 minutes. Cells were then rinsed in PBST (3% goat serum (Millipore Sigma, USA), 1% BSA, 1% PenStrep, in DPBS) and covered with 1 µg/mL DAPI solution in DPBS for 20 minutes, covered in aluminum foil. Finally, dishes were washed 3x 15 minutes with DPBS, and covered with Fluoroshield mountant (Abcam, USA). Dishes were again covered in foil and placed in 4°C overnight before fluorescent tile scan imaging the following day.

4.6 TEM imaging

2 µL AAV-MNP mixtures were pipetted to copper grid for TEM analysis to confirm adhesion. 5 µL glutaraldehyde was then added to grid to fix viruses. Grids were allowed to dry before adding 2 µL 2% uranyl acetate solution. AAV-MNP mixtures were imaged at 35k-40k total magnification using a Leo 912 TEM. Pure AAV vectors were not treated with glutaraldehyde but were treated with uranyl acetate for strong contrast in the absence of heavy metals.

4.7 Image analysis

Dishes treated with AAV-MNPs were imaged in both brightfield and fluorescent filters with a Leica DMi8 using the tile scan feature of the LAS software (Leica Microsystems, Germany). Tile scans were collected using a 5 x 28 tile field of view at 10x magnification, with 10% vertical and horizontal overlap. Fluorescent images were captured using GFP (Ex: 470/40 nm, Em: 525/50 nm, 500 ms exposure), and DAPI (Ex: 365/30 nm, Em: 447/60 nm, 50 ms exposure) fluorescent filters. Tile scans were exported from LAS software as '.tif' files and flat field corrected using the BaSiC ImageJ Plugin [46]. Each channel was then stitched together using the ImageJ FIJI Stitching Plugin [45]. The regions of the image that were outside of the dish were then manually removed using the Freehand ROI feature in FIJI. A pixel intensity threshold was then applied to each fluorescent image to identify cell presence (DAPI) and cellular expression of transduced proteins (GFP, TXR). Particle analyzer was then applied to nuclei ≥ 20 μm^2 and cells ≥ 30 μm^2. The area and locations of these cells were then exported as '.csv' files for further analysis.

4.8 Calcium dye loading and image analysis

Hippocampal cells aged 14-17 DIV were incubated with 2 mL of 2 μg/mL Calbryte AM reagent for one hour at 37C, 95% air, 5% CO2 incubator, then washed 3x with complete imaging medium (96% Neurobasal minus phenol red, 2% B-27 plus, 1% Glutamax (Thermo Fisher), 1% PenStrep). Cells were allowed to stabilize for 10 minutes following wash step in 37°C incubator. Cells were then imaged at three fixed locations (high field side, middle, low field side) within the dish using a Leica DMi8 to assess Ca^{2+}activity in the networks. Time lapse fluorescent videos were captured using a GFP fluorescent filter, 200 ms exposure, at a frame rate of 4 fps. Cells were then returned to the incubator for 10 minutes to restabilize before exposure to experimental treatment of either control, MNPs without a magnet, or MNPs + magnetic field. Cells were

exposed to these treatments for 5 minutes within the incubator before returning to the microscope to be re-imaged.

Videos were imported to ImageJ FIJI as '.lif' files. Fifty active cells (at least one visible Ca^{2+} transient event) were randomly selected as ROIs in from each video. Mean gray value was measured in each frame for all ROIs and exported as '.csv' file. These data files were assessed in MATLAB using a custom script, similar to the protocol in Beck and Kunze [34]. Briefly, for each cell, the "envelope" command was used to find the lower envelope (LE) of the intensity signal (F). The LE was then subtracted from the overall signal (F- LE = ΔF) and normalized to the median of the LE ($\Delta F/F$). Ca^{2+} events were then defined as peaks within this signal that rose above three times the standard deviation of the signal $\Delta F/F$. The average number and magnitude of Ca^{2+} events across all cells in the video were then recorded.

5 Results

5.1 Mesoscale MNP gradients are spatiotemporally tunable using permanent magnets

The first aim of the study was to identify a suitable configuration of the magnetic ring platform to achieve a temporally stable spatial gradient of MNPs mimicking the heterogenous magnetic field to which it was exposed. We utilized a 3D printed ring-shaped permanent magnet holder to exert a magnetic field with a spatially heterogeneous magnetic gradient force [33–36,47]. We first attempted to apply the GMF flush with the bottom of the dish (Figure S2), according to the original device design and function [33,34,47]. However, within the original configuration of the dish, the magnetic gradient force was too lateral, resulting in a distribution of MNPs that clustered heavily at the edge of the dish after even a brief exposure, rather than generating a gradient particle distribution.

We then elevated the culture dish above the magnetic ring (Figure 1a). This configuration

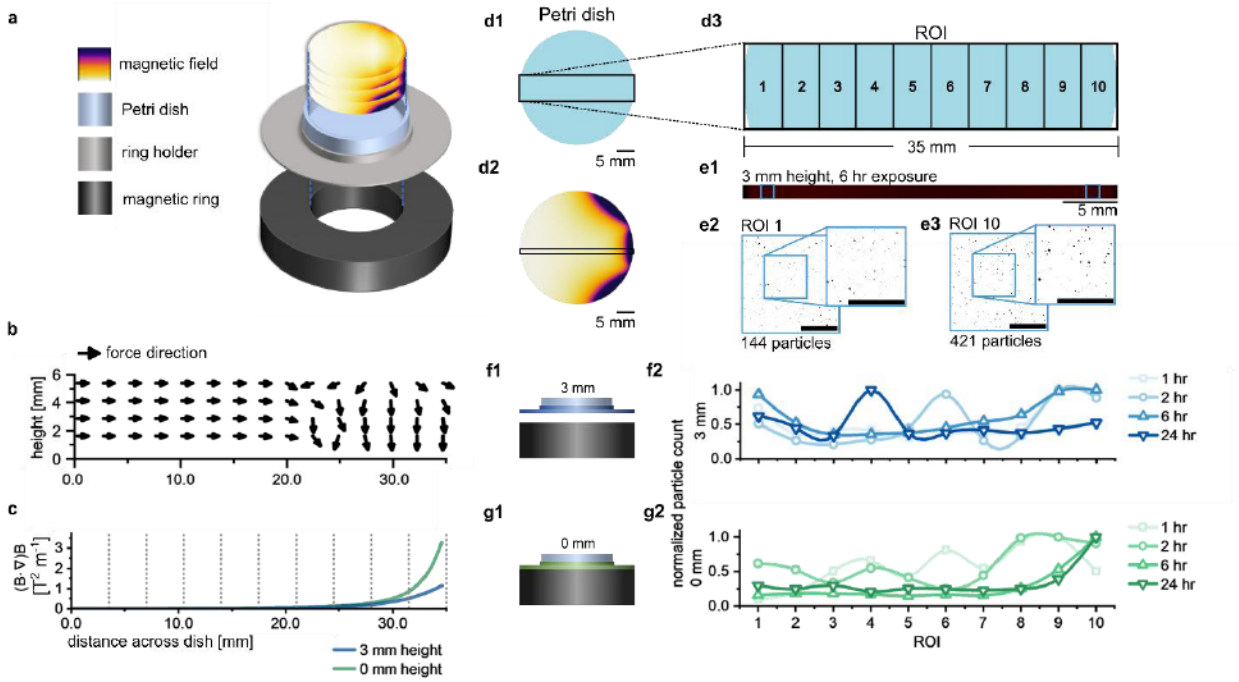


Figure 1: Magnetic nanoparticle (MNP) gradient distribution is patterned by adjusting spatiotemporal variables. a) Setup of the gradient platform: a 3D printed ABS magnetic ring provides permanent magnetic fields to a 35-mm Petri dish, secured in place by a custom-built Petri dish holder. b) COMSOL Multiphysics simulations were utilized to identify the direction of magnetic gradient force across a dish directly above the magnetic ring. c) COMSOL simulations were utilized to calculate the magnetic field strength, $(B\cdot\nabla)B$, across the center of a Petri dish directly on top (0 mm height) or lofted above (3 mm height) the magnetic ring. d1) To examine the distribution of MNPs across the dish, a tile scan of images was captured across the center of the Petri dish. d2) COMSOL simulation of magnetic field across bottom of 35 mm Petri dish at 0 mm height. Yellow = low field, ROI 1; purple = high field, ROI 10. d3) This tile scan image was then divided into ten regions of interest to assess MNP presence along the magnetic gradient. e1) Fluorescent tile scans along the magnetic gradient axis. Binarized images of fluorescent MNPs in (e2) ROI 1, low field and (e3) ROI 10, high magnetic field region. Scale bar = 250 µm. f1) Illustration of Petri dish lofted 3 mm above magnetic ring. f2) Line plots of MNP distributions in mm lofted dishes exposed to magnetic field for 1, 2, 6, or 24 hours. g1) Illustration of Petri dish lofted 0 mm above magnetic ring. g2) Line plots of MNP distributions in 0 mm lofted dishes exposed to magnetic field for 1, 2, 6, or 24 hours.

was advantageous in that MNPs were still pulled laterally, (Figure 1b) but also were halted from overconcentrating in large clusters within the high GMF by the downward pull, generating a drag force against the bottom of the dish. In effect, this generated the opposing drag forces found in studies that utilize magnetic forces to distribute nanoparticles or even cells within a liquid hydrogel [42]. We then tested the spatiotemporal effects of applying magnets from a height of 0 mm (dish flush with top of magnetic ring) or 3 mm above the top of the magnetic ring with MNPs. We utilized finite element modeling to calculate the magnetic field strengthalong the

bottom surface of the dish at each of these heights (Figure 1c). The 0 mm height resulted in a maximum magnetic field strength of approximately 3.5 T^2 m^{-1}, while the maximum field strength at 3 mm above the ring was approximately 1 T^2 m^{-1}. We utilized fluorescently-labeled MNPs to test whether these GMFs could be recapitulated as a nanoparticle distribution. Following magnetic field exposure, we captured tile scans of the 35-mm Petri dishes (Figure 1d1) along the horizontal axis of the GMF using a Leica DMi8 microscope. Although the GMF increased in both x and y directions, we only examined a central strip of the dish using this tile scan method. We therefore refer to this pseudo-one-dimensional magnetic gradient as a 1.5D gradient (Figure 1d2). We then divided the tile scans into 10 equally spaced regions of interest (ROI, Figure 1d3), and quantified the number of fluorescent MNPs (Figure 1e1) in each region x by applying an intensity threshold across the image. We were then able to use a particle analyzer to automatically count the number of MNPs in each region (Figures 1e2-1e3). This count was then normalized to the total surface area of each region to account for the rounded edges of the dish in regions 1 and 10.

We also sought to determine whether an MNP gradient could be optimized by increasing the amount of time that the dish was exposed to the magnetic field. At each time point (GMF exposure for 1, 2, 6, 24 hours), dishes lofted 3 mm above the ring (Figure 1e1) produced a distribution that did not resemble the exponential increase in magnetic field strength that was previously calculated (Figure 1e2). Maximum MNP counts were distributed across the dish, rather than near the side of the high magnetic field side near ROI 10. This indicates that the field strength was not great enough to generate the desired gradient effect. However, in dishes located at a height 0 mm above the magnetic ring (Figure 1g1), maximum field MNP distributions were shifted toward the high field region of the dish, especially following 6 or 24 hours of magnetic

field exposure (Figure 1g2). This distribution at 6 hours, rather than 1 or 2 hours of exposure would indicate that MNPs were likely pulled along the bottom of the dish, rather than being pulled quickly toward the magnetic field during their initial descent through the media. The remainder of this study utilized a 6-hour magnetic field exposure at a 0 mm height to achieve MNP gradients within the dishes.

5.2 Delayed magnetic application yields strong guided magnetofection expression gradients

Our next aim was to utilize this MNP gradient to achieve a spatially heterogenous protein expression gradient. Magnetofection is a technique that has been in use for over two decades [40,41], that exploits the negative surface charge of viral capsids or DNA plasmids to electrostatically attach these vectors to MNPs with a positive surface charge. In the original technique, viruses are mixed briefly with nanoparticles, then added to a dish or well plate sitting atop a magnetic plate. According to the theory of this method, the magnetic field concentrates virally-functionalized MNPs on adherent cells at the bottom of the dish, thus increasing the potential contacts that can be made between the viruses and the MNPs, increasing transduction rates [48]. Our study aimed to expand on this technique by utilizing the heterogeneous magnetic gradient force to guide MNP-viruses for increased transduction in specific locations within a dish of adherent cells.

To minimize off-target transduction of unattached viruses that could mask the potential gradient effect, we adapted a magnetic washing protocol from Schubert *et al.* [49,50]. Positively-charged, commercially acquired polyethylenimine (PEI)-coated MNPs (Figure S3) were mixed with adeno-associated virus (AAV) carrying a GFP gene of interest (Figure 2a) for 12 hours. AAV-PEI-MNPs were gathered by exposure to a 0.6 T permanent magnet for 10 minutes, and

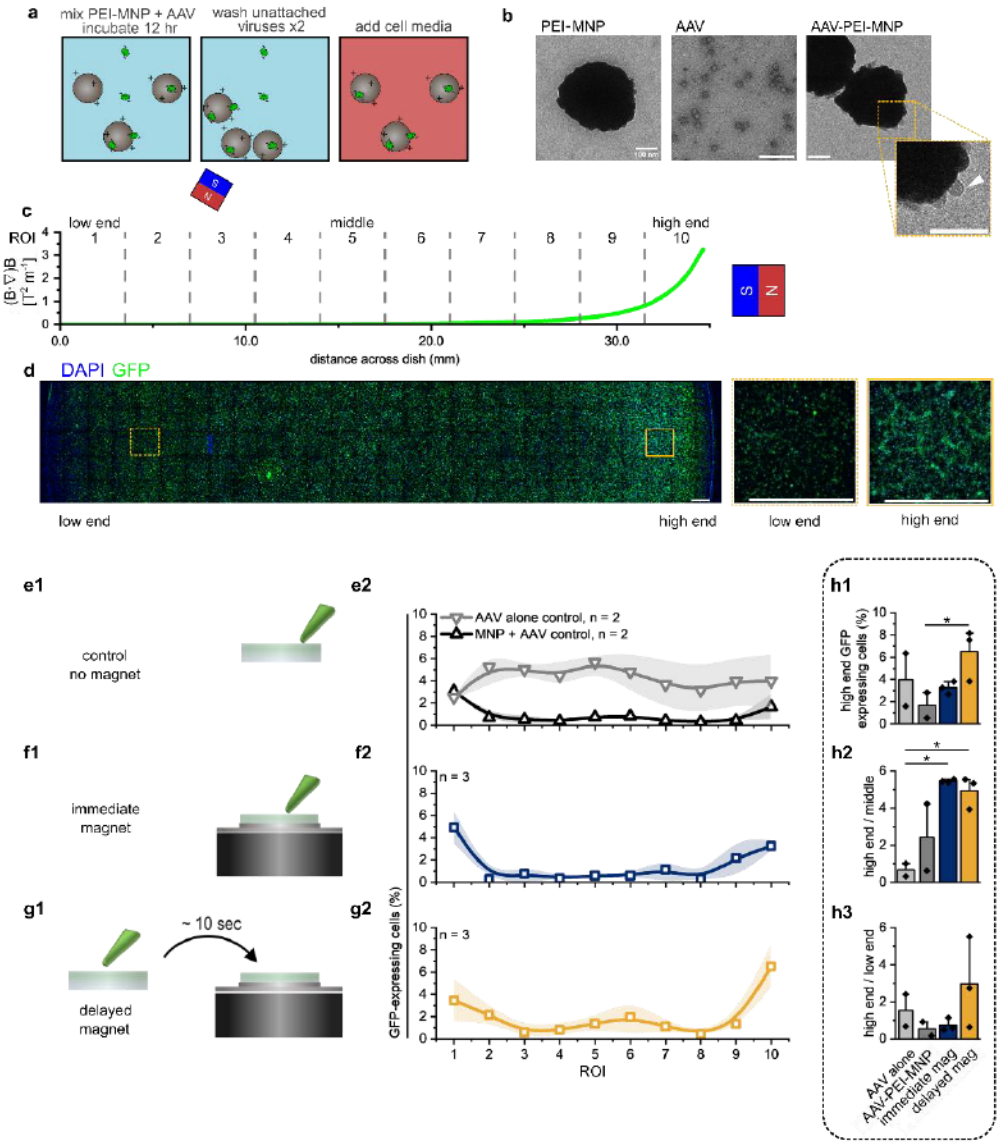


Figure 2: Guided magnetofection facilitates dish-wide protein expression gradients. a) Illustration of attachment of GFP-containing AAV vectors to positively charged PEI-coated MNPs, with magnetically assisted washing. b) TEM images of PEI-MNPs, AAV vectors, and AAV-PEI-MNPs following mixing. Scale bars = 100 nm. c) COMSOL simulation of magnetic field strength $(B\cdot\nabla)B$ across the Petri dish, magnet indicates high field side, with ROI numbers indicated. d) Fluorescent tile scan image of GFP expression across dish of primary neurons 96 hours post-transduction. Scale bars = 1 mm. e) Illustration (e1) and line graphs (e2) of GFP expression rates in control experiments. f) Illustration (f1) and line graphs (f2) of GFP expression rates in dishes with immediate magnet application. g) Illustration (g1) and line graphs (g2) of GFP expression rates in dishes with delayed (~10 seconds) magnet application. Shading = standard deviation. h) Bar plots of quantified gradient characteristics. h1) Percent of cells expressing GFP in high field ROI. h2) Ratio of GFP-expressing cells in high end ROI compared to middle of dish. h3) Ratio of GFP-expressing cells in high field ROI compared to low field ROI of dish. *: $p < 0.05$, one-sided Student's T-test.

unattached viruses were then removed by pipetting off the supernatant. We confirmed attachment of AAV to PEI-MNPs through TEM imaging (Figure 2b). We then tested whether the gradient

platform established above could facilitate protein expression gradients within a dish of primary cortical neurons. Neurons were exposed to AAV-PEI-MNPs for 24 hours, with GMF (Figure 2c) applied for the first 6 hours of exposure. Cells were then imaged 96 hours after initial transduction to allow for GFP protein translation (Figure S4). Using the same tile scanning approach as outlined above (Figure S5), we were able to visually confirm that while GFP expression was present throughout the dish, a strong increase in expression was visible near the high magnetic field strength region of the dish (Figure 2d).

We quantified the protein expression in these cells by normalizing the number of cells expressing GFP to the total number of cells present in each ROI along the dish. Control groups were either exposed to AAV vectors alone, or AAV-MNPs without an applied magnetic field (Figure 2e1). In dishes exposed to AAV alone, we saw approximately 8-10% of cells expressing GFP in each ROI. In AAV-MNP control cells, most ROIs showed a low ~2% expression rate across most regions (Figure 2e2). A slight increase was seen on either end of the dish, which was likely imaging artefact. We tested two means of applying the magnetic field. First, we added MNPs to the dish of cells while the dish was already set within the magnetic field platform (immediate magnet, Figure 2f1). This approach appeared to yield slightly higher GFP expression on the high magnetic field end of the dish (Figure 2f2). In a second experimental group, we added AAV-MNPs to cells that were not actively in the magnetic field but were moved to the field within 10 seconds of AAV-MNP addition (delayed magnet, Figure 2g1). Interestingly, this approach yielded even higher GFP expression in the high magnetic field ROI (Figure 2g2).

To quantify the expression gradients, we first compared the GFP expression rates in the high magnetic field ROI. The delayed magnet group showed increased GFP expression compared to expression in the AAV-MNP control group ($p = 0.044$, one-sided Student's T-test,

Figure 2h1). GFP expression was not significantly increased in the immediate magnet group ($p = 0.09872$). To compare the enrichment of this region to the rest of the dish, we calculated the fold change in GFP expression in the high-field region and the middle-field region. In both magnet application groups, we identified an increased ratio when compared to the AAV-alone dishes (immediate: $p = 1.88\times10^{-4}$ delayed: $p = 4.57\times10^{-3}$, Figure 2h2), but not compared to the AAV-PEI-MNP group. We also examined the fold change in expression between the high magnetic field group and the low field group but found no significant differences between either of the applied magnet groups and the control groups (Figure 2h3). These results indicate that while some guided enrichment could be achieved with immediate magnet application, delaying the application of the magnet to the dish of AAV-PEI-MNPs generated greater enrichment within the high field region.

5.3 Short-term MNP application induces minimal Ca^{2+} activity shifts

We then wanted to examine whether the application of this effective force gradient impacted neuronal Ca^{2+} dynamics. Many studies have examined the impacts of exogenously-applied forces on neuronal activity, including the dynamic influx of Calcium ions (Ca^{2+}) to the neuronal cytosol. Cell-internal NMFs have been shown to briefly increase, then decrease Ca^{2+} events of primary neurons over a sustained period of force application [47] Dynamic Ca^{2+} imaging also revealed differentiated neuronal responses to high and low magnitude external forces [51]. We therefore sought to explore whether this platform generated spatially differentiated Ca^{2+} activity responses in primary neurons due to exogenous force.

We cultured primary hippocampal cells to 14 days *in vitro* (DIV), allowing the cells to form matured networks [52,53]. Cells were then treated with Calbryte 520 AM dye to examine

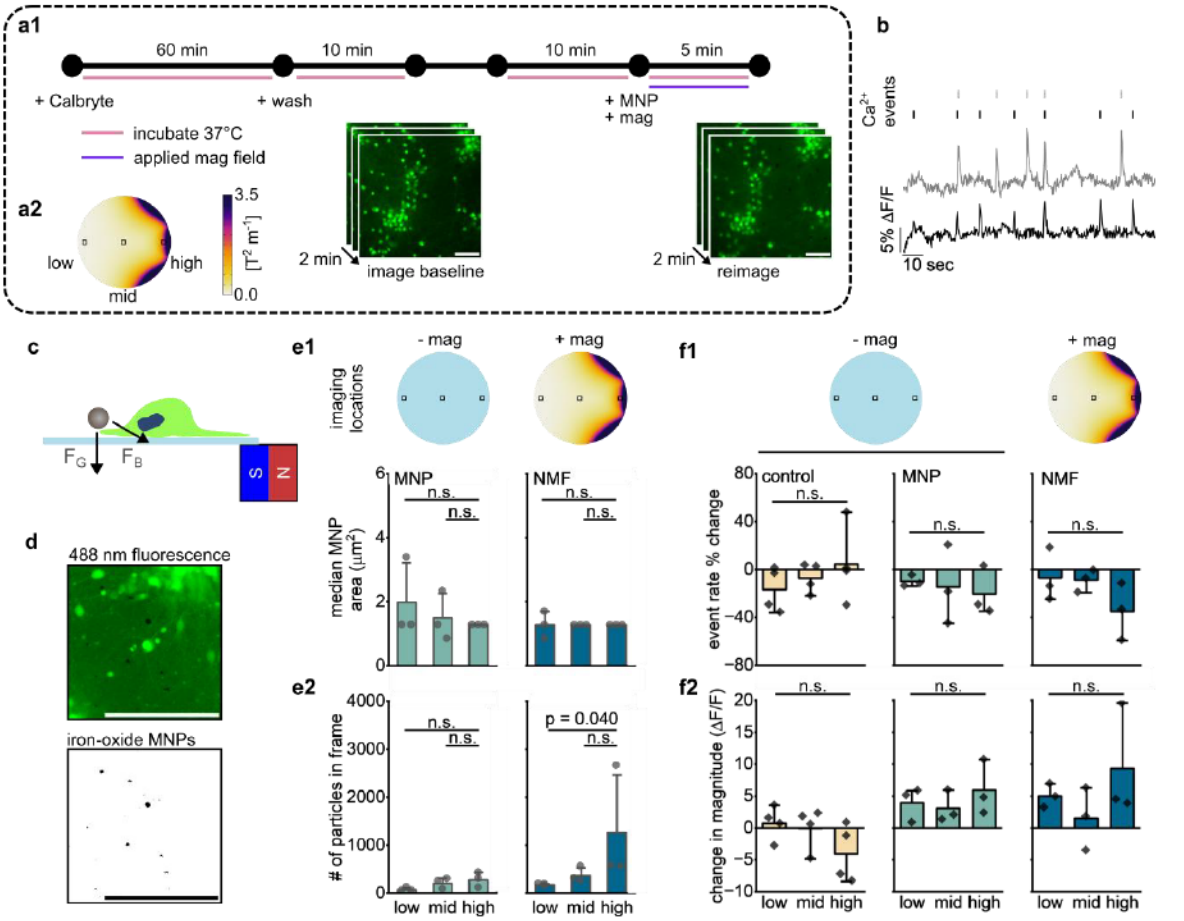


Figure 3: Short term MNP gradient force application does not significantly alter cellular Ca^{2+} dynamics. a) Experimental setup of Ca^{2+} tests. a1) Primary hippocampal neurons at 14-15 days *in vitro* (DIV) were incubated with Calbryte 520 Ca^{2+} indicator dye for one hour, then washed before taking baseline capturing Ca^{2+} dynamics for two minutes in each location. PEI-MNPs were applied with or without a magnetic field for 5 minutes prior to re-imaging to assess changes in Ca^{2+} dynamics. a2) Cells exposed to gradient magnetomechanical field (GMF) were imaged in low, mid, and high magnetic field locations. b) Example Ca^{2+} fluorescent signals (line plots) and identified spike events (raster points). c) Illustration of cell within magnetic field in the presence of PEI-MNPs, pushing on the cell *via* gravitational (F_G) and magnetic (F_B) forces. d) Fluorescent (top) and threshold-applied images (bottom) show PEI-MNP presence as dark, dense masses. e) Bar plots of MNP distribution in +MNP and + NMF mag groups assessed by median PEI-MNP cluster area (e1) and number of clusters (e2) identified in each Ca^{2+} imaging field of view. Statistics represent results of one-sided Mann-Whitney U test. f) Changes in Ca^{2+} events between baseline and post-MNP application period in control, +MNP, and + NMF groups. f1) Bar plots of change in Ca^{2+} event rates. f2) Bar plots of change in Ca^{2+} event magnitudes. Statistics represent one-way ANOVA test.

318 changes in Ca^{2+} dynamics before and after MNP and NMF application (Figure 3a1). Ca^{2+}

319 dynamics were captured in three locations corresponding to low, middle, and high GMF

320 locations (Figure 3a2) for two minutes in each location. Fluorescent Ca^{2+} dynamics were

321 extracted from 50 randomly selected cells with at least one visible event throughout the

recording period, from which we were able to calculate the mean Ca^{2+} event rate and event magnitude (Figure 3b). We hypothesized that because dense particles ($\rho \approx 5.17$ g cm^{-3}) would exert gravitationally-actuated mechanical force on the cells, as well as nanomagnetic forces (Figure 3c, Figure S6), overall responses from the cells would differ from the control group, even when a magnetic field was not applied.

From the captured time-lapse fluorescent videos, PEI-MNP clusters were visible as dark shapes that were not present in baseline videos (Figure 3d). We applied intensity thresholding to extract the number and two-dimensional size of these clusters to quantify these clusters in each video's field of view and thus quantify the concentration of MNPs in these three locations along the GMF axis. Whether a GMF was applied, median PEI-MNP cluster area did not differ significantly between imaging locations (Figure 3e1). However, we observed that when the GMF was applied, even for a short period, the number of PEI-MNP clusters was increased in the high gradient field location compared to the low gradient field location ($p = 0.04$, one-sided Mann-Whitney U-test), though not enriched compared to the middle field (Figure 3e2). Locally, NMF would therefore be increased in the region not only due to a higher GMF, but also due to a greater number of MNPs present.

We then examined how Ca^{2+} dynamics changed within these locations. In control cells, we identified non-uniform responses across locations. This is likely due to the sequential nature of the imaging protocol, rather than network effects. Imaging sequences were kept consistent across experimental groups. The overall change in Ca^{2+} event rates remained relatively close to 0 in the control groups (Figure 3f1). Ca^{2+} activity tended to decrease compared to baseline in both MNP ($p = 0.522$, one-way ANOVA) and NMF-applied groups ($p = 0.230$). In high field locations in particular, Ca^{2+} events decreased, although this difference was not statistically significant.

Where activity rates tended to decrease, MNP and NMF groups showed an increase in Ca^{2+} event magnitude (Figure 3f2). Again, these changes appeared to be most acute in the high field location but were not significantly different from the other field locations ($p = 0.344$). This data would indicate that there was not a significant difference in cellular responses generated by increased NMF.

However, we observed that the most extreme responses in NMF-applied cells appeared in the same location where the greatest number of PEI-MNPs were identified. We wondered, therefore, if the changes in Ca^{2+} dynamics could be modeled according to the amount of force applied to the cells. We calculated an approximate MNP "pressure" exerted on the local networks in each time-lapse video, including both gravitationally and magnetically actuated MNP force. We utilized ANCOVA analysis of the linear regression model and identified that while the responses in both MNP and NMF cells did not present significantly differing responses, changes in both Ca^{2+} event rates event magnitudes were significantly correlated to the overall MNP pressure force across the local network (Figure S7). Therefore, while a one-way ANOVA analysis of the responses revealed no significant effects on Ca^{2+} dynamics, these data indicate that these responses could be tuned by altering the concentration of MNPs introduced to the cells.

6 Discussion

Our work in this study aimed at developing a platform to generate a mesoscale gradient of protein expression across a large culture of cells. While groups have engineered expression gradients on the micro- or millimeter scales [16,42], we sought to generate expression gradients on the centimeter scale, which is often diffusion limited using fluidics-based techniques. Our study utilized a 3D-printed ring containing permanent NdFeB magnets to generate a gradient

distribution of MNPs, which could then be exploited to generate a gradient of intracellular protein expression by means of guided magnetofection. This technique builds on the long-established magnetofection technique, typically used to uniformly increase cellular uptake of genetic vectors.

This first required the reconfiguration of the magnetic ring assembly to induce a gradient-like nanoparticle distribution, rather than a densely clustered effect at the high magnetic field region. Commercially available nanoparticles were selected for this study to demonstrate the accessibility of this technology for We were able to achieve a gradient distribution by arranging the Petri dish above the magnetic ring, rather than within the ring, utilizing both the lateral pull of the magnetic field as well as the downward pull to induce drag. Petri dishes were raised to increasing heights above the magnetic ring and exposed to GMFs for four increasing lengths of time, then imaged across the center of the dish to assess distribution. At 0 mm height (rested atop the ring) and a minimum exposure of 6 hours, we were able to achieve a distribution of MNPs that resembled the GMF to which it was exposed.

We then utilized this system to generate a gradient of intracellular fluorescent protein expression, across a 35-mm dish of primary neurons. Intriguingly, this method was improved by a minor delay (~10 s) in the application of the magnetic field. We have considered why the delayed magnetic field would have resulted in greater GFP expression enrichment when compared to the immediate application. As MNPs can be decorated with multiple AAV, as identified through TEM imaging (Figure 2b), a single particle could contact, and induce transduction of, multiple cells as the particle is pulled within the magnetic field. In the delayed magnet group, AAV-PEI-MNPs would be able to descend toward the bottom of the dish before magnetic gradient forces were applied. We hypothesize that this positioning would allow MNPs

391 to contact more cells as they were pulled toward the high magnetic field, compared to the MNPs
392 that added to a dish actively within a magnetic field.

393 We found that the application of short-term PEI-MNP-actuated forces did not result in a
394 significant gradient effect on Ca^{2+} activity, although this effect could potentially be tuned in
395 future by altering MNP concentrations. It is unlikely that decreases in Ca^{2+} were due to
396 neurotoxicity, as PEI is often employed to mitigate the toxicity of genetic vector vehicles
397 [54,55]. The decrease in event rate is consistent with previous work on the effect of
398 nanomagnetic force on neuronal Ca^{2+} activity, which found that application of NMF over the
399 course of four minutes led to event decreases by the end of the modulation period [34] The subtle
400 responses from the neuronal networks in response to applied force may, in fact, be due to the
401 extracellular, low magnitude application of the force. We estimate that, in the high magnetic field
402 location, the median nanomagnetic force exerted by individual PEI-MNP clusters was in the low
403 piconewton range (approximately 1.3 pN per particle cluster). The majority of MNPs identified
404 were visualized in regions rich in neurites, rather than cell bodies. While Ca^{2+} activity can be
405 tuned by extracellular membrane deformations, force thresholds along neurites differ from those
406 in the soma [51]. In cortical neurons, both axons and dendrites require a higher threshold of
407 pressure to induce activity changes, at least 20 kPa, which is several orders of magnitude higher
408 than our calculations. Known mechanosensitive ion channels are often responsive to point force
409 magnitudes two orders of magnitude greater than our calculations [56]. Therefore, if the aim of a
410 study were to produce greater shifts in Ca^{2+} activity, it would likely be necessary to utilize larger
411 or more numerous MNPs to exert greater force.

412 This technology holds a great deal of potential for future work, as the study presented
413 here is inherently a proof-of-concept to expand the spatial scales to which these forces can be

414 applied to achieve spatially differentiated effects. While our study used a single field gradient,
415 we anticipate that multiple fields could be applied sequentially to achieve opposing gradients.
416 Such fields could be utilized to apply gradients of mutually inhibitory morphogens (i.e. SHH and
417 BMP gradients in neural tube formation) [57,58]. Antiparallel gradients are notoriously difficult
418 to simulate, but we anticipate that this technology offers a potential route for consistent
419 application of morphogens across a large culture of cells. Further, while our study utilizes
420 neuronal cells, gradient techniques could be applied to many other types of cells and/or tissues.
421 Bone and cartilage engineering is especially attuned to the use of mechanical forces for guided
422 growth, and the field has already shown interest in the use of nanomagnetic technology [43,59].
423 Ultimately, we believe that, while this study is limited in scope, it provides a strong avenue for
424 future work in the literal expansion *in vivo*-like of tissue and cellular culture.

425 Considerations for future use of this magnetic technology must include the potential for
426 cellular toxicity. While we did not identify particularly harmful effects in our study due to the
427 low dose of MNPs used (0.1 mg/mL), acute iron oxide toxicity can result from high
428 concentrations of MNPs [60]. Lower concentrations of nanoparticles, often uptaken by cells, can
429 be removed from the cytosol via endogenous iron clearance pathways [61,62]. Use of static,
430 permanent magnetic fields mitigates the risk of nanoparticle overheating introduced by
431 alternating magnetic field platforms. Thus, with controlled concentrations of nanoparticles and a
432 stable magnetic source, this platform provides a low-risk means of introducing multi-faceted
433 gradients within a large cell culture.

434 This study functions as a proof-of-concept that nanomagnetic forces can induce
435 gradiented distributions of protein expression within a 2D cell culture. Functionalized MNP
436 studies have drawn interest from researchers in a variety of fields, especially within neuroscience

and bone/cartilage tissue engineering. Future studies utilizing this method could utilize a more active gene of interest that could elicit a functional gradient as well. These could include downstream molecules of morphogen pathways. Further, sequential application of GMFs using antiparallel, mutually inhibitory morphogens could generate *in vivo*-like rostral/caudal or anterior/posterior gradients. This study shows the potential for the next generation of magnetofection technology to be used to further the engineering of neuronal environments.

Acknowledgments

The design and fabrication of the ForceApplicator magnetic device, as well as experimentation, was partially funded by the National Science Foundation CAREER Award (CBET-1846271). This publication was supported by the National Center for Advancing Translational Sciences of the National Institutes of Health under Award Number TL1TR002318. Materials for this study were also partially funded by MSU CATalyst GAP Fund (USEDA) no. ED19HDQ0200091, 2. The content is solely the responsibility of the authors and does not necessarily represent the official views of the National Science Foundation or the Institutes of Translational Health Sciences. The authors would like to thank C. Beck for his help with Ca^{2+} image analysis and experimental protocols and Z. Malkoç for scientific conversations and help with cell cultures.

Author contributions

Conceptualization, AK and ML; methodology, AK and ML. Formal analysis, ML; investigation, ML; writing (original draft and editing), ML; writing (review), AK and ML; funding acquisition, AK and ML; supervision, AK.

Declaration of competing financial interests

AK has also received MSU-internal research funds to use magnetic forces to advance drug screening and tissue engineering. AK and ML would like to declare inventorship on a provisional patent application associated with this research study filed by Montana State University (US Patent App. 63/446,770, filed February 17th, 2023). AK and ML are co-founders and have stock and ownership interests in NanoMagnetic Solutions, Inc. No financial support was received from NanoMagnetic Solutions, Inc. for the purpose of this research study.

Resource availability

Lead contact

Anja Kunze (anja.kunze@montana.edu)

Materials availability

This study did not generate new unique reagents.

Data and code availability

Original images, videos, raw and processed data, metadata, and codes are available upon request to the lead contact.

References

[1] I. Barkefors, S. Le Jan, L. Jakobsson, E. Hejll, G. Carlson, H. Johansson, J. Jarvius, W.P. Jeong, L.J. Noo, J. Kreuger, Endothelial cell migration in stable gradients of vascular endothelial growth factor A and fibroblast growth factor 2: Effects on chemotaxis and chemokinesis, Journal of Biological Chemistry 283 (2008). https://doi.org/10.1074/jbc.M704917200.

[2] L. Liu, B.D. Ratner, E.H. Sage, S. Jiang, Endothelial cell migration on surface-density gradients of fibronectin, VEGF, or both proteins, Langmuir 23 (2007). https://doi.org/10.1021/la701435x.

[3] P. Wu, Y. Fu, K. Cai, Regulation of the migration of endothelial cells by a gradient density of vascular endothelial growth factor, Colloids Surf. B Biointerfaces 123 (2014). https://doi.org/10.1016/j.colsurfb.2014.09.013.

[4] R.B. Campenot, Local control of neurite development by nerve growth factor, Proc. Natl. Acad. Sci. U. S. A. 74 (1977). https://doi.org/10.1073/pnas.74.10.4516.

[5] J. Lowry Curley, G.C. Catig, E.L. Horn-Ranney, M.J. Moore, Sensory axon guidance with semaphorin 6A and nerve growth factor in a biomimetic choice point model, Biofabrication 6 (2014). https://doi.org/10.1088/1758-5082/6/3/035026.

[6] S. Tang, J. Zhu, Y. Xu, A.P. Xiang, M.H. Jiang, D. Quan, The effects of gradients of nerve growth factor immobilized PCLA scaffolds on neurite outgrowth invitro and peripheral nerve regeneration in rats, Biomaterials 34 (2013). https://doi.org/10.1016/j.biomaterials.2013.05.080.

[7] M. Zagorski, Y. Tabata, N. Brandenberg, M.P. Lutolf, G. Tkačik, T. Bollenbach, J. Briscoe, A. Kicheva, Decoding of position in the developing neural tube from antiparallel morphogen gradients, Science (1979). 356 (2017). https://doi.org/10.1126/science.aam5887.

[8] J.L. Christian, Morphogen gradients in development: From form to function, Wiley Interdiscip. Rev. Dev. Biol. 1 (2012). https://doi.org/10.1002/wdev.2.

[9] K. Bartscherer, M. Boutros, Regulation of Wnt protein secretion and its role in gradient formation, EMBO Rep. 9 (2008). https://doi.org/10.1038/embor.2008.167.

[10] J. Bejoy, L. Song, Y. Zhou, Y. Li, Wnt/Yes-Associated protein interactions during neural tissue patterning of human induced pluripotent stem cells, Tissue Eng. Part A 24 (2018) 546–558.

[11] R. De Santis, F. Etoc, E.A. Rosado-Olivieri, A.H. Brivanlou, Self-organization of human dorsal-ventral forebrain structures by light induced SHH, Nat. Commun. 12 (2021). https://doi.org/10.1038/s41467-021-26881-w.

[12] J. Sipkova, K. Franze, Eph/ephrin signalling in the developing brain is regulated by tissue stiffness, BioRxiv (2024).

[13] A. Shellard, R. Mayor, Collective durotaxis along a self-generated stiffness gradient in vivo, Nature 600 (2021). https://doi.org/10.1038/s41586-021-04210-x.

[14] M. Zhu, H. Tao, M. Samani, M. Luo, X. Wang, S. Hopyan, Y. Sun, Spatial mapping of tissue properties in vivo reveals a 3D stiffness gradient in the mouse limb bud, Proc. Natl. Acad. Sci. U. S. A. 117 (2020). https://doi.org/10.1073/pnas.1912656117.

[15] N. Takata, E. Sakakura, M. Eiraku, T. Kasukawa, Y. Sasai, Self-patterning of rostral-caudal neuroectoderm requires dual role of Fgf signaling for localized Wnt antagonism, Nat. Commun. 8 (2017). https://doi.org/10.1038/s41467-017-01105-2.

[16] S.G.M. Uzel, O.C. Amadi, T.M. Pearl, R.T. Lee, P.T.C. So, R.D. Kamm, Simultaneous or sequential orthogonal gradient formation in a 3D cell culture microfluidic platform, Small 12 (2016) 612–622.

[17] Y. Tang, Q.F. Qiu, F.L. Zhang, M. Xie, W.H. Huang, Quantifying orientational regeneration of injured neurons by natural product concentration gradients in a 3D microfluidic device, Lab Chip 18 (2018). https://doi.org/10.1039/c7lc01143a.

[18] C. Beck, T. Singh, A. Farooqi, T. Venkatesh, M. Vazquez, Controlled microfluidics to examine growth-factor induced migration of neural progenitors in the Drosophila visual system, J. Neurosci. Methods 262 (2016). https://doi.org/10.1016/j.jneumeth.2015.12.012.

[19] H. Huang, L. Jiang, S. Li, J. Deng, Y. Li, J. Yao, B. Li, J. Zheng, Using microfluidic chip to form brain-derived neurotrophic factor concentration gradient for studying neuron axon guidance, Biomicrofluidics 8 (2014). https://doi.org/10.1063/1.4864235.

[20] B. Hong, P. Xue, Y. Wu, J. Bao, Y.J. Chuah, Y. Kang, A concentration gradient generator on a paper-based microfluidic chip coupled with cell culture microarray for high-throughput drug screening, Biomed. Microdevices 18 (2016). https://doi.org/10.1007/s10544-016-0054-2.

[21] A. Kunze, S. Lengacher, E. Dirren, P. Aebischer, P.J. Magistretti, P. Renaud, Astrocyte-neuron co-culture on microchips based on the model of SOD mutation to mimic ALS, Integrative Biology (United Kingdom) 5 (2013). https://doi.org/10.1039/c3ib40022k.

[22] A. Kunze, R. Meissner, S. Brando, P. Renaud, Co-pathological connected primary neurons in a microfluidic device for alzheimer studies, Biotechnol. Bioeng. 108 (2011) 2241–2245. https://doi.org/10.1002/bit.23128.

[23] D. Kilian, T. Ahlfeld, A.R. Akkineni, A. Bernhardt, M. Gelinsky, A. Lode, 3D Bioprinting of osteochondral tissue substitutes – in vitro-chondrogenesis in multi-layered mineralized constructs, Sci. Rep. 10 (2020). https://doi.org/10.1038/s41598-020-65050-9.

[24] L. Huang, J. Gao, H. Wang, B. Xia, Y. Yang, F. Xu, X. Zheng, J. Huang, Z. Luo, Fabrication of 3D scaffolds displaying biochemical gradients along longitudinally oriented microchannels for neural tissue engineering, ACS Appl. Mater. Interfaces 12 (2020) 48380–48394.

[25] N. Pei, Z. Hao, S. Wang, B. Pan, A. Fang, J. Kang, D. Li, J. He, L. Wang, 3D Printing of Layered Gradient Pore Structure of Brain-like Tissue, Int. J. Bioprint. 7 (2021). https://doi.org/10.18063/ijb.v7i3.359.

[26] M. Cadena, L. Ning, A. King, B. Hwang, L. Jin, V. Serpooshan, S.A. Sloan, 3D Bioprinting of Neural Tissues, Adv. Healthc. Mater. 10 (2021). https://doi.org/10.1002/adhm.202001600.

[27] K.E. Kador, S.P. Grogan, E.W. Dorthé, P. Venugopalan, M.F. Malek, J.L. Goldberg, D.D. D'Lima, Control of Retinal Ganglion Cell Positioning and Neurite Growth: Combining 3D Printing with Radial Electrospun Scaffolds, Tissue Eng. Part A 22 (2016). https://doi.org/10.1089/ten.tea.2015.0373.

[28] N.A. Repina, H.J. Johnson, X. Bao, J.A. Zimmermann, D.A. Joy, S.Z. Bi, R.S. Kane, D. V. Schaffer, Optogenetic control of Wnt signaling models cell-intrinsic embryogenic patterning using 2D human pluripotent stem cell culture, Development (Cambridge) 150 (2023). https://doi.org/10.1242/dev.201386.

[29] Y. Qian, Z. Yan, X. Li, S. Chen, H. Jiang, C. Chen, W.E. Yuan, C. Fan, Gradient Nanoaggregation in a Magnetically Actuated Scaffold for Multiscale Immunoregulation and Microenvironment Remodeling Accelerates Nerve and Muscle Repair, ACS Mater. Lett. 5 (2023) 580–595. https://doi.org/10.1021/acsmaterialslett.2c00684.

[30] Y. Cai, P. Wang, Y. Li, T.W. Tang, L. Zhang, H. Shu, H. Wong, Y. Li, J. Li, A.C. Arias, C. Zhang, G. Jin, Q. Huang, Z. Luo, Triple-Cue-Guided Multichannel Hydrogel Conduit to Synergistically Enhance Peripheral Nerve Repair, ACS Nano 19 (2025) 22163–22178. https://doi.org/10.1021/acsnano.5c03215.

[31] W.C. Huang, C.C. Lin, T.W. Chiu, S.Y. Chen, 3D Gradient and Linearly Aligned Magnetic Microcapsules in Nerve Guidance Conduits with Remotely Spatiotemporally Controlled Release to Enhance Peripheral Nerve Repair, ACS Appl. Mater. Interfaces 14 (2022) 46188–46200. https://doi.org/10.1021/acsami.2c11362.

[32] S.S. Shevkoplyas, A.C. Siegel, R.M. Westervelt, M.G. Prentiss, G.M. Whitesides, The force acting on a superparamagnetic bead due to an applied magnetic field, Lab Chip 7 (2007). https://doi.org/10.1039/b705045c.

[33] D. Judge, A. Kunze, Neural network growth under heterogenous magnetic gradient patterns, in: International IEEE/EMBS Conference on Neural Engineering, NER, 2019. https://doi.org/10.1109/NER.2019.8716902.

[34] C.L. Beck, A. Kunze, Parallelized Mechanical Stimulation of Neuronal Calcium Through Cell-Internal Nanomagnetic Forces Provokes Lasting Shifts in the Network Activity State, Small 21 (2025) 2406678. https://doi.org/https://doi.org/10.1002/smll.202406678.

[35] C.L. Beck, C.T. Killeen, S.C. Johnson, A. Kunze, Nanomagnetic Guidance Shapes the Structure–Function Relationship of Developing Cortical Networks, Nano Lett. 24 (2024) 13564–13573. https://doi.org/10.1021/acs.nanolett.4c03156.

[36] M.K. Landis, A. Kunze, Intra-axonal Nanomagnetic Forces Differentially Impact hTau40 Transport Dynamics in Primary Cortical and Hippocampal Neurons, ACS Nano 19 (2025) 7884–7897.

[37] K. Ino, A. Ito, H. Honda, Cell patterning using magnetite nanoparticles and magnetic force, Biotechnol. Bioeng. 97 (2007). https://doi.org/10.1002/bit.21322.

[38] A. Ito, H. Akiyama, Y. Kawabe, M. Kamihira, Magnetic force-based cell patterning using Arg-Gly-Asp (RGD) peptide-conjugated magnetite cationic liposomes, J. Biosci. Bioeng. 104 (2007). https://doi.org/10.1263/jbb.104.288.

[39] K. Ino, A. Ito, H. Honda, Cell patterning using magnetite nanoparticles and magnetic force, Biotechnol. Bioeng. 97 (2007). https://doi.org/10.1002/bit.21322.

[40] F. Scherer, M. Anton, U. Schillinger, J. Henke, C. Bergemann, A. Krüger, B. Gänsbacher, C. Plank, Magnetofection: Enhancing and targeting gene delivery by magnetic force in vitro and in vivo, Gene Ther. 9 (2002). https://doi.org/10.1038/sj.gt.3301624.

[41] C. Plank, U. Schillinger, F. Scherer, C. Bergemann, J.-S. Rémy, F. Krötz, M. Anton, J. Lausier, J. Rosenecker, The Magnetofection Method: Using Magnetic Force to Enhance Gene Delivery, 384 (2003) 737–747. https://doi.org/10.1515/BC.2003.082.

[42] C. Li, J.P. Armstrong, I.J. Pence, W. Kit-Anan, J.L. Puetzer, S. Correia Carreira, A.C. Moore, M.M. Stevens, Glycosylated superparamagnetic nanoparticle gradients for osteochondral tissue engineering, Biomaterials 176 (2018). https://doi.org/10.1016/j.biomaterials.2018.05.029.

[43] L. Zwi-Dantsis, B. Wang, C. Marijon, S. Zonetti, A. Ferrini, L. Massi, D.J. Stuckey, C.M. Terracciano, M.M. Stevens, Remote Magnetic Nanoparticle Manipulation Enables the Dynamic Patterning of Cardiac Tissues, Advanced Materials 32 (2020). https://doi.org/10.1002/adma.201904598.

[44] M. Marcus, G. Indech, N. Vardi, I. Levy, A. Smith, S. Margel, O. Shefi, A. Sharoni, Magnetic Organization of Neural Networks via Micro-Patterned Devices, Adv. Mater. Interfaces 7 (2020). https://doi.org/10.1002/admi.202000055.

[45] S. Preibisch, S. Saalfeld, P. Tomancak, Globally optimal stitching of tiled 3D microscopic image acquisitions, Bioinformatics 25 (2009). https://doi.org/10.1093/bioinformatics/btp184.

[46] T. Peng, K. Thorn, T. Schroeder, L. Wang, F.J. Theis, C. Marr, N. Navab, A BaSiC tool for background and shading correction of optical microscopy images, Nat. Commun. 8 (2017). https://doi.org/10.1038/ncomms14836.

[47] C.L. Beck, A.M. Kirby, S. Roberts, A. Kunze, Multimodal Characterization of Cortical Neuron Response to Permanent Magnetic Field Induced Nanomagnetic Force Maps, ACS Nano 18 (2024) 34630–34645. https://doi.org/10.1021/acsnano.4c09542.

[48] S. Arora, G. Gupta, S. Singh, N. Singh, Advances in Magnetofection & − Magnetically Guided Nucleic Acid Delievery:a Review, Journal of Pharmaceutical Technology, Research and Management 1 (2013). https://doi.org/10.15415/jptrm.2013.11002.

[49] R. Schubert, S. Herzog, S. Trenholm, B. Roska, D.J. Müller, Magnetically guided virus stamping for the targeted infection of single cells or groups of cells, Nat. Protoc. 14 (2019) 3205–3219.

[50] R. Schubert, S. Trenholm, K. Balint, G. Kosche, C.S. Cowan, M.A. Mohr, M. Munz, D. Martinez-Martin, G. Fläschner, R. Newton, Others, Virus stamping for targeted single-cell infection in vitro and in vivo, Nat. Biotechnol. 36 (2018) 81–88.

[51] B.M. Gaub, K.C. Kasuba, E. Mace, T. Strittmatter, P.R. Laskowski, S.A. Geissler, A. Hierlemann, M. Fussenegger, B. Roska, D.J. Müller, Neurons differentiate magnitude and location of mechanical stimuli, Proc. Natl. Acad. Sci. U. S. A. 117 (2020). https://doi.org/10.1073/pnas.1909933117.

[52] E. Biffi, G. Regalia, A. Menegon, G. Ferrigno, A. Pedrocchi, The influence of neuronal density and maturation on network activity of hippocampal cell cultures: A methodological study, PLoS One 8 (2013). https://doi.org/10.1371/journal.pone.0083899.

[53] M. Ichikawa, K. Muramoto, K. Kobayashi, M. Kawahara, Y. Kuroda, Formation and maturation of synapses in primary cultures of rat cerebral cortical cells: an electron microscopic study, Neurosci. Res. 16 (1993). https://doi.org/10.1016/0168-0102(93)90076-3.

[54] Y. Cui, X. Li, K. Zeljic, S. Shan, Z. Qiu, Z. Wang, Effect of PEGylated Magnetic PLGA-PEI Nanoparticles on Primary Hippocampal Neurons: Reduced Nanoneurotoxicity and

Enhanced Transfection Efficiency with Magnetofection, ACS Appl. Mater. Interfaces 11 (2019). https://doi.org/10.1021/acsami.9b15014.

[55] G.P. Tang, J.M. Zeng, S.J. Gao, Y.X. Ma, L. Shi, Y. Li, H.P. Too, S. Wang, Polyethylene glycol modified polyethylenimine for improved CNS gene transfer: Effects of PEGylation extent, Biomaterials 24 (2003). https://doi.org/10.1016/S0142-9612(03)00029-2.

[56] A. Tay, D. Di Carlo, Magnetic Nanoparticle-Based Mechanical Stimulation for Restoration of Mechano-Sensitive Ion Channel Equilibrium in Neural Networks, Nano Lett. 17 (2017) 886–892. https://doi.org/10.1021/acs.nanolett.6b04200.

[57] R. Vetter, D. Iber, Precision of morphogen gradients in neural tube development, Nature Communications 2022 13:1 13 (2022) 1145-. https://doi.org/10.1038/s41467-022-28834-3.

[58] M. Zagorski, Y. Tabata, N. Brandenberg, M.P. Lutolf, G. Tkačik, T. Bollenbach, J. Briscoe, A. Kicheva, Decoding of position in the developing neural tube from antiparallel morphogen gradients, Science (1979). 356 (2017) 1379–1383. https://doi.org/10.1126/science.aam5887.

[59] J. Xu, Y. Cui, X. Sun, Z. Chen, M. Liu, X. Wang, P. Li, Y. Fan, Continuous magnetic-gradient hydrogel with augmented mechanical span and reverse-directional polysaccharides distribution for integrated repair of osteochondral defects, Compos. B Eng. 298 (2025) 112361. https://doi.org/10.1016/j.compositesb.2025.112361.

[60] R.P. Badman, S.L. Moore, J.L. Killian, T. Feng, T.A. Cleland, F. Hu, M.D. Wang, Dextran-coated iron oxide nanoparticle-induced nanotoxicity in neuron cultures, Sci. Rep. 10 (2020). https://doi.org/10.1038/s41598-020-67724-w.

[61] N. Spotorno, J. Acosta-Cabronero, E. Stomrud, B. Lampinen, O.T. Strandberg, D. van Westen, O. Hansson, Relationship between cortical iron and tau aggregation in Alzheimer's disease, Brain 143 (2020). https://doi.org/10.1093/brain/awaa089.

[62] A. Carocci, A. Catalano, M.S. Sinicropi, G. Genchi, Oxidative stress and neurodegeneration: the involvement of iron, BioMetals 31 (2018). https://doi.org/10.1007/s10534-018-0126-2.